

CrossMark
click for updatesCite this: *RSC Adv.*, 2015, 5, 5725

Enhanced visible-light-induced photocatalytic performance of a novel ternary semiconductor coupling system based on hybrid Zn–In mixed metal oxide/g-C₃N₄ composites†

Meng Lan, Guoli Fan, Lan Yang and Feng Li*

Hybrid composites of Zn–In mixed metal oxides (ZnIn-MMO) and g-C₃N₄ were synthesized by a facile thermal decomposition of Zn–In layered double hydroxide (ZnIn-LDH) and melamine mixture precursors. The structural and optical properties of the ZnIn-MMO/g-C₃N₄ composites were characterized by powder X-ray diffraction, transmission electron microscopy, UV-vis diffuse reflectance spectroscopy, X-ray photoelectron spectra, photoluminescence spectra, electron spin resonance and transient absorption spectra. The results indicated that ZnIn-MMO nanoparticles were well distributed over the surface of the g-C₃N₄ sheets formed *in situ*. Compared with pristine ZnIn-MMO, the as-synthesized ZnIn-MMO/g-C₃N₄ nanohybrids showed stronger absorption in the visible light region. Furthermore, the ZnIn-MMO/g-C₃N₄ composite with a g-C₃N₄ amount of 36 wt% exhibited significantly enhanced photodegradation activity for Rhodamine B under visible light irradiation, in comparison with pure g-C₃N₄ and ZnIn-MMO, which was attributable to the unique heterostructure of the ternary semiconductor coupling system composed of g-C₃N₄, In₂O₃ and ZnO in the composites, facilitating efficient transportation and separation of the photogenerated electron–hole pairs and thus the continuous generation of reactive oxygen species. The present finding provides a simple approach for fabricating new types of visible-light-induced g-C₃N₄-based semiconductor composite photocatalysts for pollutant degradation in advanced oxidation processes.

Received 14th July 2014
Accepted 12th December 2014

DOI: 10.1039/c4ra07073a

www.rsc.org/advances

1. Introduction¹

Over the past two decades, increasing attention has been drawn to the photocatalytic degradation of organic pollutants over semiconductor photocatalysts like the most widely employed TiO₂ and ZnO for the remediation of hazardous wastes and contaminated groundwater,^{1–3} which is becoming a solar energy-based green technology. In particular, visible-light-induced photocatalysts are attracting considerable interest because of their high efficiency in utilizing solar energy.^{4–6} TiO₂, however, exhibits low efficiency in utilizing solar energy, because of its relatively large band gap. Recently, heterostructured semiconductor photocatalysts formed by coupling two kinds of metal oxides together, such as ZnO/TiO₂, ZnO/In₂O₃, and NiO/TiO₂,^{7–9} were found to be able to extend their optional expense and thus exhibit good photocatalytic activity by improving the separation efficiency of electron–hole pairs.

In recent years, a novel graphitic carbon nitride (g-C₃N₄) with the graphite-like sp²-bonded C–N structure and the optical band gap of about 2.7 eV, which possesses out-standing thermal, electrical and optical characteristics as a nontoxic metal-free semiconductor,^{10,11} is attracting much attention due to its promising visible-light-driven photocatalytic performance for water splitting or organic pollutant decomposition.^{12–15} Nevertheless, low quantum efficiency and fast recombination of photogenerated electron–hole pairs of such kind of metal-free semiconductor still limit greatly the enhancement of its photocatalytic activity. Therefore, some heterostructured g-C₃N₄-based photocatalysts coupling with other semiconductors, such as g-C₃N₄–Ag₂O,¹⁶ g-C₃N₄–ZnWO₄,¹⁷ g-C₃N₄–WO₃,¹⁸ g-C₃N₄–Bi₂WO₆ (ref. 19) and so on,^{20–23} have been developed widely, taking into account the fact that photogenerated electron–hole pairs can transfer between g-C₃N₄ and other semiconductors thus enhancing the photo conversion efficiency *via* the depression of charge recombination.

On the other hand, among new generation of heterogeneous photocatalysts, layered double hydroxides (LDHs, [M_{1–x}^{II}M_x^{III}(OH)₂]^{x+}(A^{n–})_{x/n}·mH₂O) are very much promising photocatalysis materials for pollutant degradation. LDHs are a family of highly ordered two-dimensional layered anionic clays

State Key Laboratory of Chemical Resource Engineering, Beijing University of Chemical Technology, P. O. BOX 98, Beijing, 100029, P. R. China. E-mail: lifeng@mail.buct.edu.cn; Fax: +86-10-64425385; Tel: +86-10-64451226

† Electronic supplementary information (ESI) available: Additional experimental results. See DOI: 10.1039/c4ra07073a

that consist of positively charged brucite $[\text{Mg}(\text{OH})_2]$ -like layers containing alternatively distributed divalent and trivalent cations in the sheets and charge balancing interlayer anions between the layers.^{24–26} Calcination of LDHs at intermediate temperatures (450–600 °C) can form poorly crystallized mixed metal oxides (MMOs). In comparison with other MMOs, LDH-derived MMOs have two advantages: (i) a uniform distribution of metal cations at the atomic level without a segregation of “lakes” of separate cations within the brucite-like layers, which ensures high homogeneity in LDH precursors, facilitates the formation of highly dispersed MMOs through the topological transform upon calcination; (ii) components of MMOs can be adjusted in a controllable manner. Especially, the appropriate incorporation of photo-active components (*e.g.*, Zn, Cr or Fe) into LDHs, followed by calcination, can afford a variety of semiconductor photocatalysts with a band gap normally in the range from 2.0 to 3.4 eV.^{27–31} For example, it was reported that calcined Zn- or Fe-containing LDHs could be used as photocatalysts for photo-degradation of organic pollutants, taking advantage of the formation of highly dispersed ZnO or Fe₂O₃ semiconductor phases.^{27–29} Similar to ZnO, these LDHs-derived photocatalysts are mainly driven by UV light irradiation. Recently, our group found that Zn- and In-containing MMOs fabricated by thermal decomposition of corresponding LDH precursors exhibited good visible-light-induced photocatalytic properties.^{30,31} Nevertheless, the photocatalytic activity of LDHs-derived MMOs is still low and needs to be further modified.

As for photocatalysts, an increase of the lifetime of photo-generated charge carriers is always of crucial importance in enhancing the photocatalytic efficiency. In this work, we for the first time synthesized new hybrids of ZnIn-*MMO* and *g-C₃N₄* (ZnIn-*MMO/g-C₃N₄*) by a simple thermal decomposition of ZnIn-LDH and melamine mixture precursors. As-synthesized ZnIn-*MMO/g-C₃N₄* composites combined the unique properties of ternary *g-C₃N₄*, ZnO and In₂O₃ semiconductors, and a synergistic effect between ZnIn-*MMO* and *g-C₃N₄* contributed to significantly improved photocatalytic activity in degrading organic Rhodamine B (RhB) dye under visible light irradiation. Furthermore, the reactive species for the dye degradation were determined, and the mechanism for enhanced photo-degradation activity of ZnIn-*MMO/g-C₃N₄* composites was discussed. To the best of our knowledge, there has been no report about ternary semiconductor coupling system composed of *g-C₃N₄* and other semiconductor components to promote visible-light-induced photocatalytic performance until now. The ZnIn-*MMO* hybridized with *g-C₃N₄* might produce a high-performance photocatalytic material for organic pollutant removal.

2. Materials and methods

2.1. Materials

All reagents were of analytical grade and purchased from Beijing Chemical Reagent Ltd. without further purification. Deionized water was used in all experiments.

2.2. Synthesis of ZnIn-*MMO/g-C₃N₄* composites

ZnIn-LDH precursor was prepared by coprecipitation method. Zn(NO₃)₂·6H₂O and In(NO₃)₃·4H₂O with the Zn/In molar ratio of 3.0 were dissolved in 30 mL deionized water to form a clear salt solution ($[\text{Zn}^{2+}] = 0.15 \text{ M}$; $[\text{In}^{3+}] = 0.05 \text{ M}$). Subsequently, 50 mL alkali solution of NaOH (0.24 M) and Na₂CO₃ (0.1 M) was added drop-wise into the above salt solution under vigorous stirring at room temperature. The pH value of resulting solution was adjusted to 10.0 by further titration of NaOH solution (0.24 M). The suspension was aged at 60 °C for 6 h, and then filtered and washed with distilled water until the pH of the filtrates was nearly 7. The solid were dried at 60 °C for 16 h in a vacuum oven. The obtained ZnIn-LDH was mixed with melamine by grinder, where the mass ratio of melamine to ZnIn-LDH is 1, 3 and 5. Then the mixture was calcined under N₂ gas flow (flow rate: 60 standard-state cm³ min⁻¹) at 550 °C for 4 h at a heating rate of 5 °C min⁻¹. The obtained composite was denoted as *x*-*MMO/C₃N₄*, where *x* means the mass ratio of melamine to ZnIn-LDH. According to the total mass loss obtained by thermogravimetric analysis, the relative amount of *g-C₃N₄* in composites increases from 1-*MMO/C₃N₄* (about 16 wt%) to 3-*MMO/C₃N₄* (about 36 wt%) and 5-*MMO/C₃N₄* (about 48 wt%). For comparative study, pure *g-C₃N₄* or ZnIn-*MMO* was prepared without the addition of ZnIn-LDH or melamine under identical experimental conditions.

2.3. Characterization

Powder X-ray diffraction (XRD) data were collected at room temperature on a Shimadzu XRD-6000 diffractometer with graphite-filtered Cu K α source ($\lambda = 0.15418 \text{ nm}$), 40 kV, 30 mA. Room-temperature Fourier transform infrared (FT-IR) spectra were recorded on a Vector 22 spectrometer from Bruker. Transmission electron microscopy (TEM) and high-resolution transmission electron microscopy (HRTEM) observations were carried out on a JEOL JEM-2010 electron microscope at an accelerating voltage of 200 kV. Solid state UV-vis diffuse absorption spectra were recorded on a Shimadzu UV-2501PC spectrometer equipped with an integrating sphere attachment at room temperature and in air. X-ray photoelectron spectra (XPS) was recorded on a Thermo VG ESCALAB2201-XL X-ray photoelectron spectrometer at a base pressure of $2 \times 10^{-9} \text{ Pa}$ using Al K α X-ray (1486.6 eV) as the excitation source. Binding energies were calibrated based on the graphite C 1s peak at 284.6 eV. N₂ adsorption-desorption isotherms of samples were obtained using a Micromeritics ASAP 2020 sorptometer apparatus. The specific surface areas were calculated from the multipoint Brunauer-Emmett-Teller (BET) method. The total organic carbon (TOC) was determined using an Apollo 9000 TOC Analyzer (Terkmar Dohrmann Co.). The quantitative information of the active radicals were investigated by a Bruker electron spin resonance (ESR) 300E. 5,5-Dimethylpyrroline-*N*-oxide (DMPO) was used as spin-trapping reagent. Photoluminescence (PL) spectra were acquired at room temperature using a FLUOROMAX-4 spectrophotometer. Transient absorption spectra (TAS) were recorded on an Edinburgh LP920 spectrophotometer (Edinburgh Instruments). All samples were

excited by using 355 nm output with pulse energies of 1.5 mJ per pulse from an OPO pumped by an Nd:YAG laser (10 Hz, 8 ns) (Continuum Surelite). On-line software of the LP920 spectrophotometer was used to analyse the data. Photocurrent-time measurements were performed on an electro-chemical analyzer (CHI660C, CHI Shanghai, Inc.) in a standard three-electrode configuration with a Pt foil as the counter electrode and a saturated calomel electrode (SCE) as the reference electrode. Irradiation proceeded with a 300 W Xe arc lamp with a UV cut off filter (>420 nm) filter. Na₂SO₄ (0.1 M) aqueous solution was used as the electrolyte. The working electrode was prepared as follows: 10 mg sample was dispersed in 1 mL of ethanol by sonication, and the resulting slurry was spread onto an indium-tin oxide glass electrode with an exposed area of 4 cm². The transient photocurrent of the photocatalysts responded to the light on and off was located at 0.0 V to stimulate the same working condition as that of the photocatalysis reaction system.

2.4. Photocatalytic test

The photocatalytic activities of photocatalysts were evaluated by measuring the degradation of RhB in aqueous solution under visible light (>420 nm). The visible light source was a 300 W Xe arc lamp (PLS-SXE 300UV) with a 420 nm cut-off filter and $I = 20$ A. Typically, 100 mL aqueous solution of RhB (10 ppm) containing 0.1 g catalyst sample was ultrasonically dispersed in a quartz beaker for 10 min, and then the suspension was vigorously agitated for 60 min in the dark to reach adsorption-desorption equilibrium before the irradiation. Then the suspension was stirred and exposed to visible light irradiation, and the concentration of RhB was determined by absorbance at 553 nm in UV-vis absorption spectrum during the photodegradation process. A blank reaction was carried out following the same procedure without adding any catalyst. Additionally, other three organic pollutants, acid red 87 (AR 87), methylene blue (MB) and methyl orange (MO), were used to investigate the photocatalytic performance of the synthesized catalyst. In the cycling tests, the mixture solution was centrifuged to remove the catalyst after the reaction. The catalyst was washed with ethanol and deionized water, and finally dried at 70 °C for 24 h. Then, fresh dye, as well as the recovered catalyst, was employed in the repeated reactions.

3. Results and discussion

3.1. Characterization of ZnIn-MMO/g-C₃N₄ nano hybrids

As shown in Fig. 1, the XRD patterns of pure ZnIn-LDH precursor display four characteristic diffractions at 2θ angles below 40° corresponding to (003), (006), (012) and (015) planes of hydroxalcalite-like materials (JCPDS no. 15-0087) and two characteristic (110) and (113) lines at high 2θ of about 61°.³² In addition, the broad characteristic diffractions can be attributed to the low crystalline nature of LDH phase originating from the incorporation of In³⁺ ions with the large ionic radius of 0.081 nm into the brucite-like layers.

Fig. 2 presents the XRD patterns of as-synthesized ZnIn-MMO/g-C₃N₄ nano hybrids with different content of g-C₃N₄,

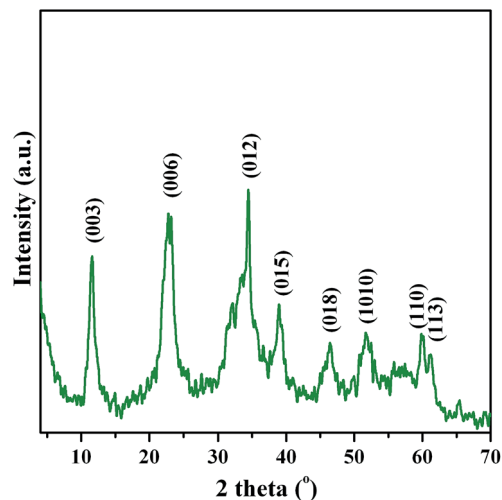


Fig. 1 XRD patterns of pure ZnIn-LDH precursor.

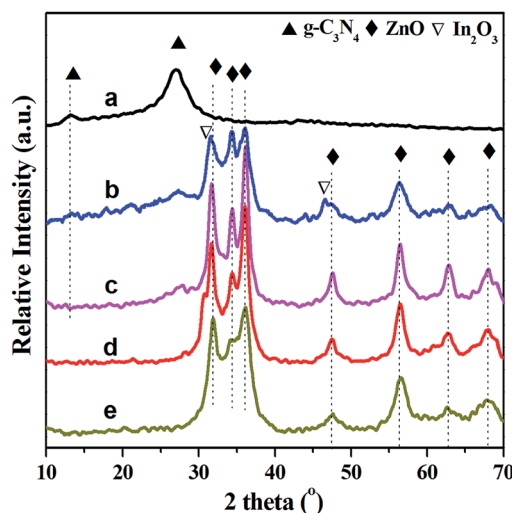


Fig. 2 XRD patterns of pure g-C₃N₄ (a), 5-MMO/C₃N₄ (b), 3-MMO/C₃N₄ (c) 1-MMO/C₃N₄ (d) and ZnIn-MMO (e).

pure g-C₃N₄ and ZnIn-MMO. It is found that the XRD patterns of pure g-C₃N₄ present characteristic (002) and (100) diffractions at 2θ of about 13.2° and 27.4°, respectively, which correspond to the interplanar staking peaks of aromatic systems and the inter-layer structural packing.²⁰ All ZnIn-MMO/g-C₃N₄ composites display intensive characteristic diffractions indexed as the hexagonal wurtzite structure for ZnO (JCPDS no. 36-1451). Note that no characteristic diffractions related to g-C₃N₄ phase are observed in the 1-MMO/C₃N₄ with the smallest amount of g-C₃N₄. However, with the increasing of g-C₃N₄ amount, the characteristic diffractions of g-C₃N₄ phase can be found more clearly. In addition, the characteristic diffractions of In₂O₃ phase only are found in the 5-MMO/C₃N₄, indicative of the better crystalline nature of ZnIn-MMO. As expected, pristine ZnIn-MMO only presents the characteristic diffractions of ZnO phase. As a result, it is reasonably assumed that the existence of a large amount of g-C₃N₄ in ZnIn-MMO/g-C₃N₄ composites may

improve the crystallization of In_2O_3 . In addition, FT-IR spectra (see ESI, Fig. S1†) suggest the coexistence of $g\text{-C}_3\text{N}_4$ and ZnIn- MMO components in composites. The aforementioned results confirm the successful hybridization of ZnIn- MMO with $g\text{-C}_3\text{N}_4$.

The morphology and structure of composites were characterized by TEM. As can be seen from Fig. 3a, pure $g\text{-C}_3\text{N}_4$ prepared by thermal decomposition of melamine at 550°C shows a rippled two-dimensional morphology and paper-like structure, which is the analogue of crumpled graphene.³³ Typically, in the case of 3- $\text{MMO}/\text{C}_3\text{N}_4$ composite, many dark aggregates of ZnIn- MMO nanoparticles with the size of *ca.* 20–40 nm are well distributed over the surface of $g\text{-C}_3\text{N}_4$ nanosheets (Fig. 3b), suggestive of the good affinity between them. A typical HRTEM image (Fig. 3c) depicts the lattice fringes with two interplanar distances of about 0.261 nm and 0.326 nm corresponding to the (002) plane of ZnO phase and the (002) plane of $g\text{-C}_3\text{N}_4$ phase in the 3- $\text{MMO}/\text{C}_3\text{N}_4$ composite. Both ZnO nanocrystallites and amorphous zones coming from In_2O_3 domains are with coherent interfaces. However, for pristine ZnIn- MMO , severely agglomerated grains composed of large particles are observed (Fig. 3d), due to the absence of the spatial confinement. As a result, $g\text{-C}_3\text{N}_4$ *in situ* formed through thermal decomposition of melamine can act as an excellent support for ZnO nanoparticles and amorphous In_2O_3 grains, leading to the successful fabrication of hybrid ZnIn- $\text{MMO}/g\text{-C}_3\text{N}_4$ composites.

XPS measurements were carried out to understand the surface/near-surface chemical states of C, N, Zn and In species for the samples. Fig. 4a depicts the C 1s XPS of $g\text{-C}_3\text{N}_4$, 3- $\text{MMO}/\text{C}_3\text{N}_4$ and ZnIn- MMO . In the case of $g\text{-C}_3\text{N}_4$, the strong C 1s peak at 288.1 eV is related to the coordination between carbon atoms and three nitrogen atoms in the $g\text{-C}_3\text{N}_4$ lattice,^{12,34} while the peak at 284.6 eV, corresponding to C–C coordination, is due to carbon-containing contaminations. Only one peak located at 284.6 eV is observed in the C 1s spectrum of ZnIn- MMO . 3- $\text{MMO}/\text{C}_3\text{N}_4$ composite also presents two C 1s peaks at 288.1

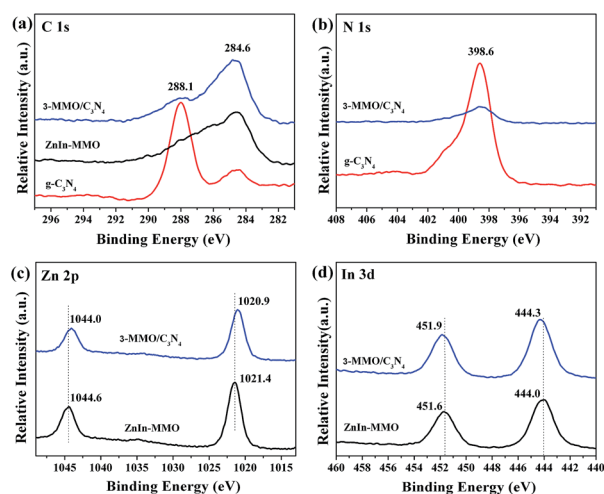


Fig. 4 XPS of C 1s (a), N 1s (b), Zn 2p (c) and In 3d (d) for samples.

and 284.6 eV, indicating the existence of graphitic carbon nitride. As shown in Fig. 4b, similar to $g\text{-C}_3\text{N}_4$, 3- $\text{MMO}/\text{C}_3\text{N}_4$ composite presents N 1s peak at 398.6 eV,³⁵ which is another characteristic peak of $g\text{-C}_3\text{N}_4$ originating from the C=N–C coordination. Fig. 4c and d show the Zn 2p and In 3d spectra of 3- $\text{MMO}/\text{C}_3\text{N}_4$ and ZnIn- MMO . Compared with those for ZnIn- MMO , however, the binding energy values of Zn 2p and In 3d for 3- $\text{MMO}/\text{C}_3\text{N}_4$ shift to the higher and lower values, respectively, which should be ascribed to the charge transfer between ZnO, In_2O_3 and $g\text{-C}_3\text{N}_4$ due to the interaction of $g\text{-C}_3\text{N}_4$ with ZnO and In_2O_3 components resulting in inner shift of Zn 2p and In 3d orbits and thus the electronic interaction between them in composites.

The UV-vis diffuse reflection spectra of $g\text{-C}_3\text{N}_4$, ZnIn- $\text{MMO}/g\text{-C}_3\text{N}_4$ and ZnIn- MMO are shown in Fig. 5. As observed in Fig. 5, the absorption edge of ZnIn- MMO appears at about 430 nm. The band gap energy (E_g) of the sample, which is calculated from the intercept of UV-vis spectra using the equation: $E_g = 1240/\lambda$,³⁶ is about 2.98 eV. As expected, $g\text{-C}_3\text{N}_4$ displays photo absorption from ultraviolet to visible light, and its band

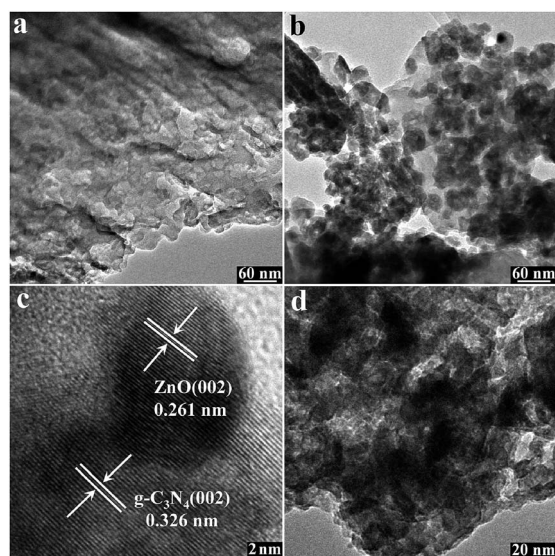


Fig. 3 TEM images of pure $g\text{-C}_3\text{N}_4$ (a), 3- $\text{MMO}/\text{C}_3\text{N}_4$ (b) and ZnIn- MMO (d); HRTEM image of 3- $\text{MMO}/\text{C}_3\text{N}_4$ (c).

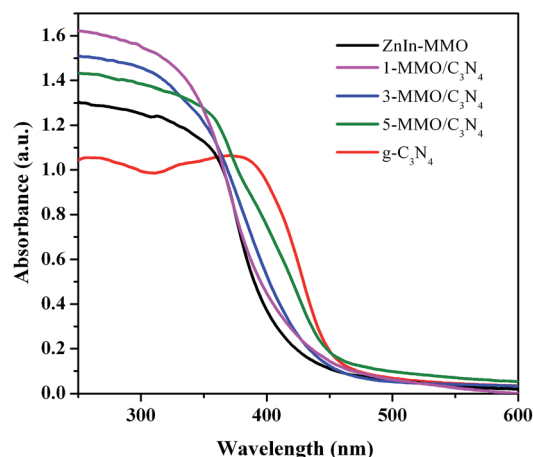


Fig. 5 UV-vis diffuse absorption spectra of different samples.

gap absorption edge is around 460 nm, corresponding to the band energy of about 2.7 eV. It can be seen that, compared with pristine ZnIn-MMO, the absorption wavelength range of ZnIn-MMO/g-C₃N₄ composites extends towards visible light and the intensity of visible light absorption also increases with the increasing g-C₃N₄ amount. The calculated E_g value of ZnIn-MMO/g-C₃N₄ composites is about 2.90 eV for 1-MMO/C₃N₄, 2.83 eV for 3-MMO/C₃N₄ and 2.75 eV for 5-MMO/C₃N₄, respectively, which are located between that of g-C₃N₄ and ZnIn-MMO and inversely vary with the g-C₃N₄ amount. The above result indicates that dispersing ZnIn-MMO on the g-C₃N₄ surface leads to the enhanced photo absorption in the visible light, which is important for the visible-light photocatalytic application.

3.2. Photocatalytic performance

Usually, the photocatalytic process is based on the generation of electron-hole pairs, thus leading to redox reactions with species adsorbed on the surface of catalysts. Considering that hybrid ZnIn-MMO/g-C₃N₄ composites exhibit stronger visible light absorption and possess more exposed active adsorption sites and photocatalytic reaction centers originating from better dispersion of ZnIn-MMO nanoparticles, as compared with ZnIn-MMO, visible-light-driven photocatalytic performance of ZnIn-MMO/g-C₃N₄ composites was investigated.

To demonstrate the photoactivity of different catalysts for the degradation of organic pollutants, the photocatalytic degradation of RhB experiments was carried out under visible light irradiation. As shown in Fig. 6A, the concentrations of the RhB solution are almost unchanged in the absence of any catalyst or in the presence of pristine ZnIn-MMO. Also, the degradation rate of RhB is slow over g-C₃N₄, and the photodegradation percentage is about 65% after 60 min irradiation. It is found that all ZnIn-MMO/g-C₃N₄ composites show enhanced photocatalytic activity, in comparison with ZnIn-MMO. With the increase of g-C₃N₄ content from 16 to 36 and 48 wt%, the removal rate of RhB over ZnIn-MMO/g-C₃N₄ increases from 29% to 100%, and then decreases to 83% after 60 min irradiation. Meanwhile, temporal evolution of the spectral changes during the photo-degradation of RhB mediated over a representative 3-MMO/C₃N₄ sample (see ESI, Fig. S2†) reveals a gradual decrease in the intensity of the strong absorption band at 553 nm for RhB aqueous solutions during the photo-assisted degradation, indicating that the RhB dye molecules have been destroyed after 60 min irradiation. Therefore, the photocatalytic activity increases in accordance with the following order: 1-MMO/C₃N₄ < g-C₃N₄ < 5-MMO/C₃N₄ < 3-MMO/C₃N₄. The highest photodegradation efficiency is achieved over 3-MMO/C₃N₄ with 100% of RhB removal.

In the case of 1-MMO/C₃N₄ composite, a less amount of g-C₃N₄ component inevitably gives rise to less visible light absorption, leading to the relatively lower photodegradation activity, compared with pure g-C₃N₄. As for 5-MMO/C₃N₄ catalyst, a severe self agglomeration of g-C₃N₄ phase can be observed (see ESI, Fig. S3†). Therefore, an excess amount of g-C₃N₄ component in composite is not beneficial to the mutual coupling between g-C₃N₄ and ZnIn-MMO, which would result in

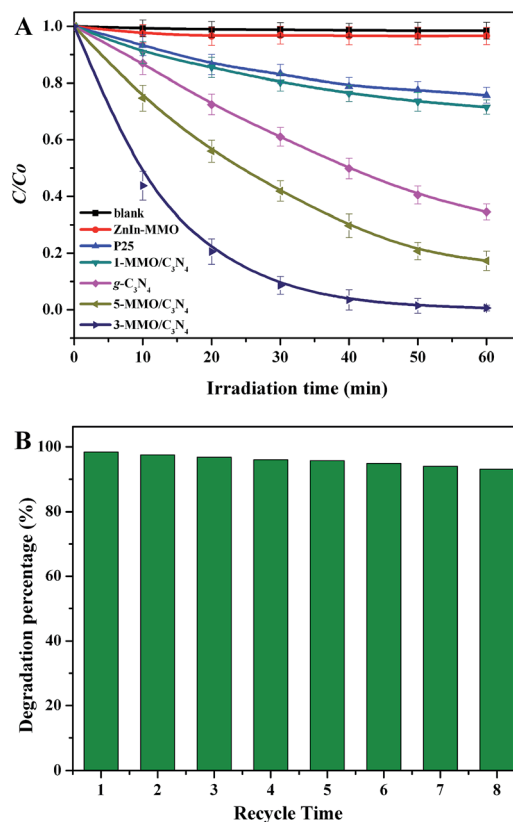


Fig. 6 Photodegradation of RhB (A) monitored as the normalized concentration change vs. irradiation time under visible light irradiation over different samples; (B) cycling runs of 3-MMO/C₃N₄ in the photodegradation of RhB.

lowly efficient photogenerated charge separation, in spite of a smaller band gap. This fact clearly denotes that the photocatalytic activity of ZnIn-MMO/g-C₃N₄ is closely related to a synergistic effect between g-C₃N₄ and ZnIn-MMO. In addition, commercially available standard Degussa P25 was used as a reference photocatalyst. It is found that the degradation percentage over P25 is only about 25%, much lower than those over ZnIn-MMO/g-C₃N₄ photocatalysts. Further, it is found that the photodegradation process of RhB over photocatalysts obeys pseudo-first-order kinetics model (see ESI, Fig. S4†). As listed in Table 1, 3-MMO/C₃N₄ shows the highest reaction rate constant (k) value among ZnIn-MMO/g-C₃N₄ photocatalysts, which is significantly higher than those over ZnIn-MMO and g-C₃N₄.

Table 1 Reaction rate constants of RhB photodegradation over different photocatalysts

Photocatalyst	S_{BET}^a (m ² g ⁻¹)	k^b (h ⁻¹)
g-C ₃ N ₄	7.0	1.08
ZnIn-MMO	38.5	0.05
1-MMO/C ₃ N ₄	39.2	0.36
3-MMO/C ₃ N ₄	39.5	5.04
5-MMO/C ₃ N ₄	38.0	1.80

^a BET surface area. ^b Reaction rate constant.

On the other hand, since the photocatalytic reaction occurs mainly at the interface between the photocatalyst and the target dyestuff, the photocatalyst with higher surface areas usually can provide more accessible active sites. However, the BET analysis reveals the specific surface areas of all ZnIn- $\text{MMO}/\text{g-C}_3\text{N}_4$ catalysts are almost equal (Table 1). This result suggests that the difference in the photocatalytic activity is not related to the specific surface area in the present ZnIn- $\text{MMO}/\text{g-C}_3\text{N}_4$ catalyst system.

To further investigate the photocatalytic activity, the TOC experiment was carried out. After 60 min irradiation, the removal efficiency of TOC over 1- $\text{MMO}/\text{C}_3\text{N}_4$, $\text{g-C}_3\text{N}_4$, 5- $\text{MMO}/\text{C}_3\text{N}_4$ and 3- $\text{MMO}/\text{C}_3\text{N}_4$ catalysts is about 18, 37, 46 and 57%, respectively, implying that the degradation of RhB over the above catalysts probably produces a large amount of carbon dioxide. More importantly, 3- $\text{MMO}/\text{C}_3\text{N}_4$ composite maintains excellent photocatalytic activity with above 95% degradation percentage of RhB after recycling for eight times (Fig. 6B). Since UV-vis diffuse adsorption spectra of 3- $\text{MMO}/\text{C}_3\text{N}_4$ almost keep unchanged before use and after eight cycles (See ESI, Fig. S5[†]), the slight decrease in the photodegradation percentage should be ascribed to a trace loss of 3- $\text{MMO}/\text{C}_3\text{N}_4$ catalyst during the operating process. The aforementioned results lead to the conclusion that as-synthesized ZnIn- $\text{MMO}/\text{g-C}_3\text{N}_4$ photocatalysts are very effective and stable visible-light-induced photocatalysts for the degradation of RhB molecules.

Other three typical organic pollutants (AR87, MB and MO) were used to investigate the catalytic performance of 3- $\text{MMO}/\text{C}_3\text{N}_4$ catalyst. As shown in Fig. 7A, after 60 min visible light irradiation, the degradation percentages for colored AR87, MB and MO reach about 90%, 86% and 82%, respectively, indicative of the excellent photocatalytic performance for the degradation of organic pollutants. In addition, considering the fact that some dyes can be self-sensitized under visible light,^{37,38} colorless 2,4,6-trichlorophenol (TCP) pollutant was used to further verify the independent efficiency of 3- $\text{MMO}/\text{C}_3\text{N}_4$ photocatalyst excluding the effect of self-sensitization of RhB under visible light. As shown in Fig. 7B, the degradation percentage for 2,4,6-trichlorophenol is about 48% after 60 min irradiation, much higher than that of P25, suggesting that the self-sensitization of dyes does not play an important role for high efficiency of hybrid ZnIn- $\text{MMO}/\text{g-C}_3\text{N}_4$ photocatalysts.

The above results demonstrate that the visible-light photocatalytic performances of $\text{g-C}_3\text{N}_4$ can be greatly enhanced by the combination of $\text{g-C}_3\text{N}_4$ and ZnIn- MMO . Especially, 3- $\text{MMO}/\text{C}_3\text{N}_4$ composite with the $\text{g-C}_3\text{N}_4$ amount of 36 wt% exhibits the highest photocatalytic activity and maintains excellent reusability under visible-light irradiation.

3.3. Mechanism of photocatalytic activity

It is well known that high energy photogenerated electron-hole pairs can form two important reactive oxygen species in the photocatalytic process including superoxide radical ($\text{O}_2^{\cdot-}$) and hydroxyl radical (OH^{\cdot}). In order to examine the effect of reactive oxygen species in the degradation of RhB, benzoquinone and *tert*-butyl alcohol (*t*-BuOH) as scavengers of $\text{O}_2^{\cdot-}$ and OH^{\cdot} were

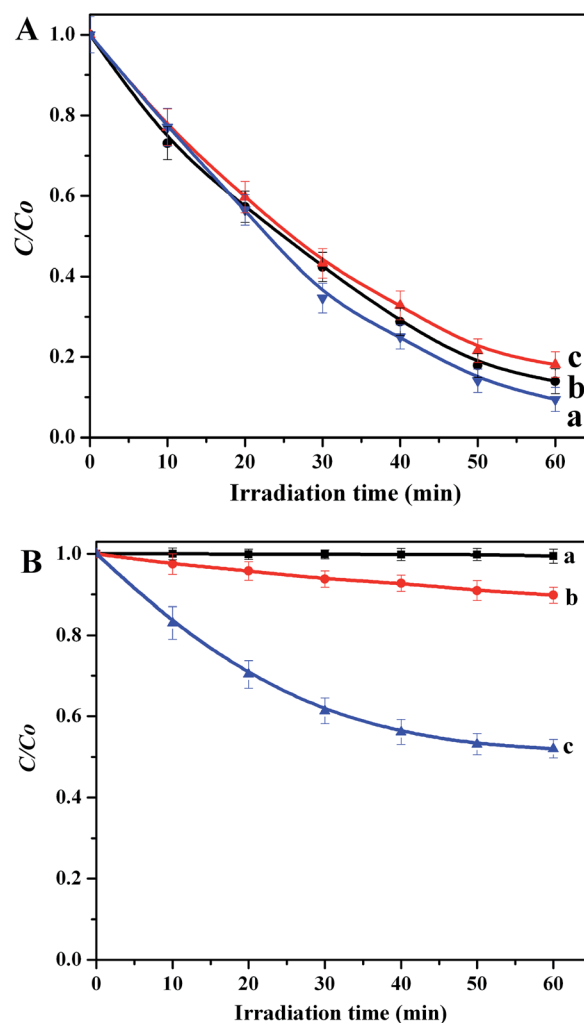


Fig. 7 Photocatalytic degradation of organic pollutants over 3- $\text{MMO}/\text{C}_3\text{N}_4$ catalyst as a function of reaction time. Colored dyes (A): AR87 (a), MB (b) and MO (c); colorless TCP (B): without catalyst (a), Degussa P25 (b) and 3- $\text{MMO}/\text{C}_3\text{N}_4$ (c).

added to the solutions separately.^{39,40} As shown in Fig. 8, the degradation percentage of RhB decreases to about 76% by the addition of benzoquinone after 60 min irradiation, while the degradation percentage of RhB decreases dramatically to about 28% in the presence of *t*-BuOH.

In order to further confirm the generation of active OH^{\cdot} and $\text{O}_2^{\cdot-}$ radicals in the photodegradation process, ESR technique using DMPO as a spin-trapping reagent were performed. As shown in Fig. 9, four characteristic peaks of DMPO- OH^{\cdot} with an intensity ratio of 1 : 2 : 2 : 1 appear in the cases of ZnIn- MMO , $\text{g-C}_3\text{N}_4$ and 3- $\text{MMO}/\text{C}_3\text{N}_4$ after visible light irradiation,⁴¹ while four nearly equal-intensity peaks of DMPO- $\text{O}_2^{\cdot-}$ are observed.⁴² No signals are observed in the dark, suggesting that visible light should be indispensable to the generation of OH^{\cdot} and $\text{O}_2^{\cdot-}$ radicals on the catalyst surface. And, the peak intensities of DMPO- OH^{\cdot} and DMPO- $\text{O}_2^{\cdot-}$ for 3- $\text{MMO}/\text{C}_3\text{N}_4$ are much higher than those for ZnIn- MMO and $\text{g-C}_3\text{N}_4$. As a result, the above

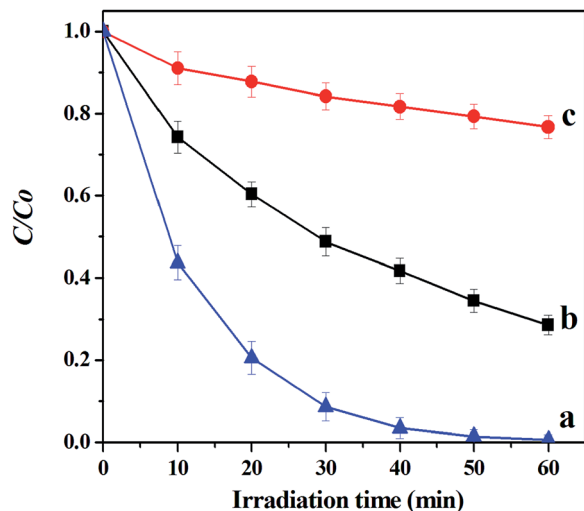


Fig. 8 Photodegradation (A) of RhB over 3- $\text{MMO}/\text{C}_3\text{N}_4$: alone (a) and with the introduction of 1 mM benzoquinone (b) and 10 mM t -BuOH (c).

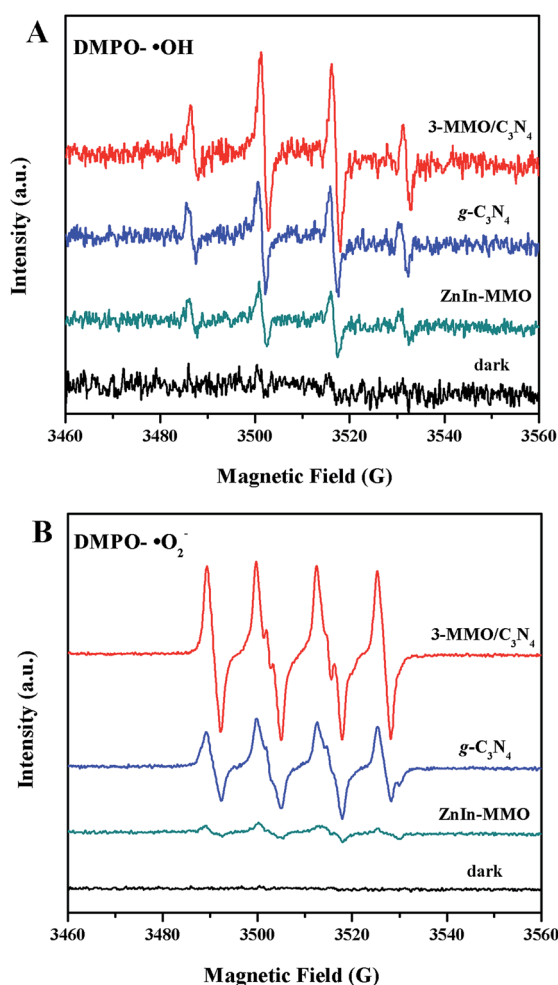


Fig. 9 DMPO spin-trapping ESR spectra for: DMPO- $\cdot\text{OH}$ in aqueous (A), DMPO- $\cdot\text{O}_2^-$ in dimethyl sulfoxide (DMSO) (B). Conditions: $[\text{DMPO}] = 0.1 \text{ mol L}^{-1}$, $[\text{catalyst}] = 1 \text{ g L}^{-1}$, Xe lamp, room temperature.

results demonstrate that two kinds of $\cdot\text{OH}$ and $\cdot\text{O}_2^-$ radicals are effective active oxidizing species in the photoreaction process.

The formation of $\cdot\text{OH}$ radical was also detected by PL technique using terephthalic acid (TA) as a probe reagent instead of RhB in the photocatalytic test.⁴³ It is well known that TA may react readily with $\cdot\text{OH}$ radical to quantitatively produce a strong fluorescent product, 2-hydroxyterephthalic acid (TAOH), and thus the PL intensity of TAOH is proportional to the amount of $\cdot\text{OH}$ radicals. As shown in Fig. 10, based on the PL intensity of TAOH ($\lambda_{\text{ex}} = 315 \text{ nm}$), the amount of the produced $\cdot\text{OH}$ radicals increase in accordance with the following order: $\text{ZnIn-MMO} < 1\text{-MMO}/\text{C}_3\text{N}_4 < g\text{-C}_3\text{N}_4 < 5\text{-MMO}/\text{C}_3\text{N}_4 < 3\text{-MMO}/\text{C}_3\text{N}_4$ under visible light irradiation for 30 min, which agrees well with their photocatalytic activity.

It is generally appreciated that efficient separation of photo-generated electron-hole pairs in photocatalysts is of much importance for photocatalytic activity.^{31,32} In the present hybrid $\text{ZnIn-MMO}/g\text{-C}_3\text{N}_4$ photocatalyst system, 3- $\text{MMO}/\text{C}_3\text{N}_4$ catalyst exhibits much higher photocatalytic activity than pure C_3N_4 and ZnIn-MMO , suggestive of more efficient separation of photo-generated charges in the composite. In order to determine the electron-hole recombination kinetics of ZnIn-MMO , $g\text{-C}_3\text{N}_4$ and 3- $\text{MMO}/\text{C}_3\text{N}_4$ photocatalysts, transient-absorption (pump-probe) spectroscopic (TAS) measurements were carried out. As shown Fig. 11, the temporal TAS profiles are perfectly fitted by a single exponential decay function, which yields the time constants of 97.8 ns for ZnIn-MMO , 130.3 ns for $g\text{-C}_3\text{N}_4$, and 165.1 ns for 3- $\text{MMO}/\text{C}_3\text{N}_4$. The larger time constant for 3- $\text{MMO}/\text{C}_3\text{N}_4$ further verifies slower electron-hole recombination kinetics, which is beneficial to the transfer and separation of the photo-generated electron-hole pairs between the interface of ZnIn-MMO and $g\text{-C}_3\text{N}_4$ in $\text{ZnIn-MMO}/g\text{-C}_3\text{N}_4$ photocatalysts. In addition, PL spectra of pure $g\text{-C}_3\text{N}_4$ and 3- $\text{MMO}/\text{C}_3\text{N}_4$ composite at an excitation wavelength of 366 nm (See ESI, Fig. S6†) further indicate that the recombination of the photo-generated electrons and holes may be inhibited greatly due to highly

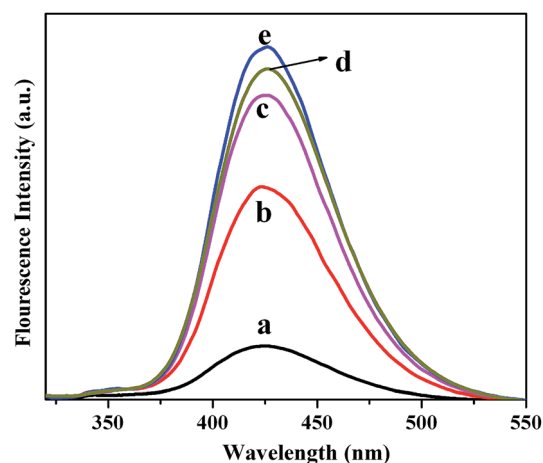


Fig. 10 Room-temperature PL spectra (B) of TAOH from reaction solution without addition of RhB in the presence of TA ($5 \times 10^{-4} \text{ M}$) with a concentration of $2 \times 10^{-3} \text{ M}$ NaOH after 30 min irradiation: (a) ZnIn-MMO , (b) $1\text{-MMO}/\text{C}_3\text{N}_4$, (c) $g\text{-C}_3\text{N}_4$, (d) $5\text{-MMO}/\text{C}_3\text{N}_4$, and (e) $3\text{-MMO}/\text{C}_3\text{N}_4$.

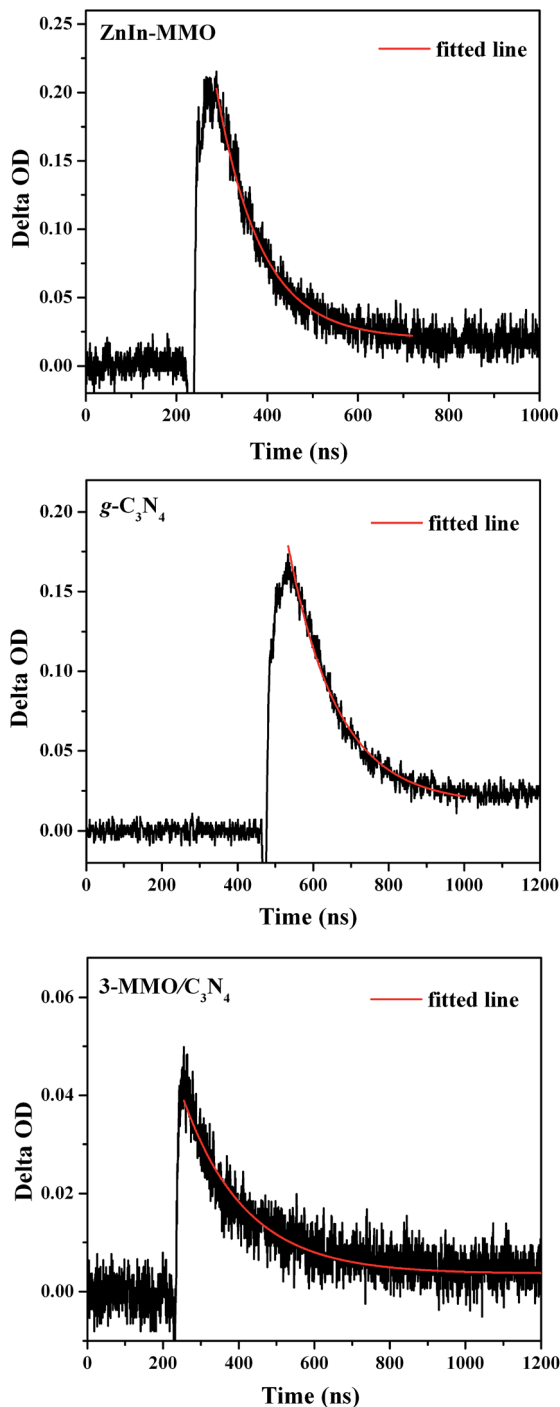


Fig. 11 Temporal TAS profiles of photocatalysts (pumped at 355 nm and probed at 500 nm).

hybridized nanostructure. The above results confirm that a slower electron-hole recombination process occurs in the 3- $\text{MMO}/\text{C}_3\text{N}_4$, accounting for the significantly improved photocatalytic activity in the degradation of RhB.

To further investigate the electronic interaction between ZnIn- MMO and $\text{g-C}_3\text{N}_4$, the transient photocurrent response *versus* time was recorded with three on-off cycles of intermittent visible-light irradiation. As shown in Fig. 12, prompt

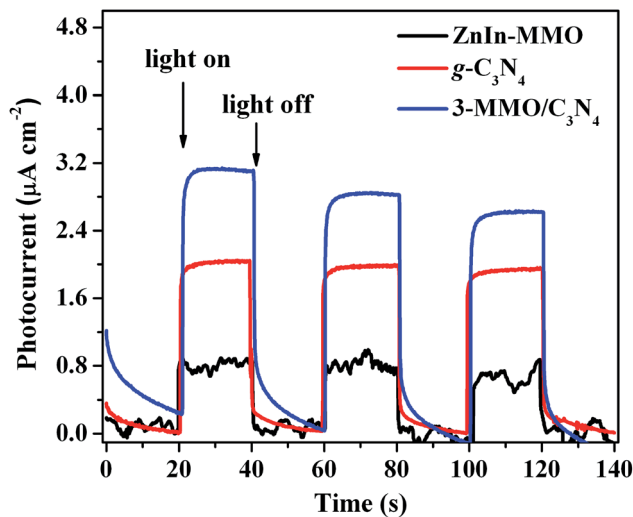


Fig. 12 Photocurrent profiles of ZnIn- MMO , $\text{g-C}_3\text{N}_4$ and 3- $\text{MMO}/\text{C}_3\text{N}_4$.

photocurrent generation is obtained during on and off cycles of illumination and the change of both “on” and “off” currents is nearly vertical. Under visible light irradiation, the photocurrent over 3- $\text{MMO}/\text{C}_3\text{N}_4$ is much higher than that over $\text{g-C}_3\text{N}_4$ and ZnIn- MMO . The photocurrent enhancement of 3- $\text{MMO}/\text{C}_3\text{N}_4$ is attributed to the enhanced separation and transfer of photo-induced electron-hole pairs originating from the intimate contact at the interface between ZnIn- MMO nanoparticles and the $\text{g-C}_3\text{N}_4$ sheets, which is benefit to the enhancement of the photocatalytic activity in ZnIn- $\text{MMO}/\text{g-C}_3\text{N}_4$ systems.

Usually, the fast intrinsic recombination of photogenerated electron-hole pairs results in low catalytic activity. Based on the above experimental results, in the present composite system of ZnIn- MMO and $\text{g-C}_3\text{N}_4$, a synergistic effect between ZnIn- MMO nanoparticles and $\text{g-C}_3\text{N}_4$ sheet plays a crucial role in photocatalytic degradation of RhB. Firstly, the good deposition of ZnIn- MMO nanoparticles on the surface of the $\text{g-C}_3\text{N}_4$ sheets can effectively inhibit the aggregation of ZnIn- MMO , leading to the formation of unique hybrid nanostructure. Secondly, according to the previous reports, the redox potential of both conduction band (CB) ($E_{\text{CB}} = -1.3$ eV vs. NHE) and valence band (VB) ($E_{\text{VB}} = +1.4$ eV vs. NHE) of $\text{g-C}_3\text{N}_4$ are more negative than those of the CB ($E_{\text{CB}} = -0.63$ eV vs. NHE) and VB ($E_{\text{VB}} = +2.17$ eV vs. NHE) of In_2O_3 and the CB ($E_{\text{CB}} = -0.5$ eV vs. NHE) and VB ($E_{\text{VB}} = +2.7$ eV vs. NHE) of ZnO.^{22,44} A scheme for the separation and transport of photogenerated electron-hole pairs at the $\text{g-C}_3\text{N}_4$ and ZnIn- MMO interface is shown in Fig. 13. When ZnIn- MMO and $\text{g-C}_3\text{N}_4$ couple together to form a heterostructure, $\text{g-C}_3\text{N}_4$ and amorphous In_2O_3 formed can be excited under visible light irradiation and generate excited electrons in the CB, since the band edges of both $\text{g-C}_3\text{N}_4$ and In_2O_3 lie in the visible region. Meanwhile, the photogenerated holes remain at VBs of $\text{g-C}_3\text{N}_4$ and In_2O_3 after migration of excited electrons. In addition, photogenerated electrons quickly transfer from the relatively high CB bottom of $\text{g-C}_3\text{N}_4$ directly into the neighboring CB bottom of In_2O_3 ; while the holes generated in the VB

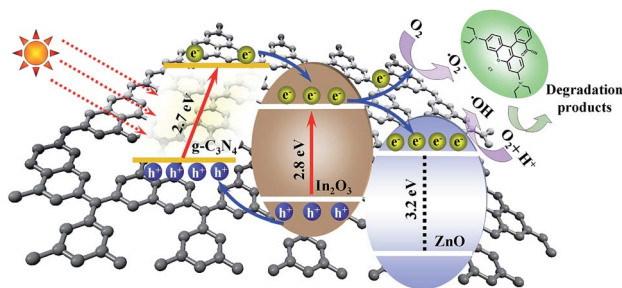


Fig. 13 Proposed mechanism of charge separation and photocatalytic activity over ZnIn-MMO/g-C₃N₄ photocatalyst under visible light irradiation.

of In₂O₃ can conveniently transfer to the VB of g-C₃N₄. On the other hand, due to the wide band gap, ZnO cannot be excited under visible light irradiation. However, ZnO nanocrystallites in contact with In₂O₃ components can act as electron traps facilitating the electron-hole separation. Namely, the photo-generated electrons can easily migrate to the surface of ZnO. As a result, the above charge transfer may reduce the recombination of the photogenerated electrons and holes of and greatly increase the photocatalytic activity of ZnIn-MMO/g-C₃N₄ photocatalysts. This efficient separation of photogenerated electron-hole pairs driven by band potentials between g-C₃N₄, ZnO and In₂O₃ semiconductors is not reported until now.

In the course of photocatalytic degradation of dyes, the electrons on ZnO can be scavenged by the adsorbed molecular O₂ to yield the superoxide radical anion $\cdot\text{O}_2^-$, due to more negative reduction potentials of g-C₃N₄, In₂O₃ and ZnO, compared with O₂/ $\cdot\text{O}_2^-$ ($E^0(\text{O}_2/\cdot\text{O}_2^-) = -0.33 \text{ eV vs. NHE}$).⁴⁵ The formed $\cdot\text{O}_2^-$ can take part in the oxidation process of dye molecules.⁴⁶ Further, due to more positive reduction potential of O₂/H₂O₂ (0.695 eV vs. NHE) than that of ZnO, O₂ in the reaction solution can react with electrons and hydrogen ions to produce H₂O₂, which may capture electrons to generate $\cdot\text{OH}$ radical. The formed $\cdot\text{OH}$ radicals directly oxidize organic pollutants.⁴⁶ However, the photogenerated holes remaining at VBs of g-C₃N₄ and In₂O₃ can not oxidize H₂O₂ to form $\cdot\text{OH}$ radical, due to more positive oxidation potential of 2.72 eV vs. NHE (OH, H⁺/H₂O) than that of g-C₃N₄ and In₂O₃.⁴⁷ In a way, photoinduced holes on the VB of g-C₃N₄ (h⁺) are probably charged with the RB molecules or the degraded RhB segments to generate degradation products.

4. Conclusions

In summary, novel hybrid ZnIn-MMO/g-C₃N₄ composite photocatalysts were synthesized by a facile thermal decomposition of ZnIn-LDH and melamine precursors. Under visible light irradiation, ZnIn-MMO/g-C₃N₄ photocatalyst with the g-C₃N₄ amount of 36 wt% exhibited significantly enhanced photocatalytic activity in the degradation of RhB, in comparison with pure g-C₃N₄ and ZnIn-MMO, which was ascribed to the novel ternary heterostructured coupling system composed of g-C₃N₄, In₂O₃ and ZnO semiconductor components. A synergistic effect

between ZnIn-MMO and g-C₃N₄ could facilitate the efficient transportation and separation of the photogenerated charge carriers in composite under visible light irradiation. Furthermore, the heterostructure improved the stability of the ZnIn-MMO nanoparticles on the surface of the g-C₃N₄ sheets. The as-synthesized g-C₃N₄-based photocatalyst composites can be regarded as a sort of promising material for further applications in advanced oxidation process utilizing visible light.

Acknowledgements

We thank gratefully the financial support from 973 Program (2011CBA00506), National Natural Science Foundation of China and Program of Beijing Engineering Center for Hierarchical Catalysts.

Notes and references

- 1 S. Yang, C. Sun, X. Li, Z. Gong and X. Quan, *J. Hazard. Mater.*, 2010, **175**, 258–266.
- 2 A. B. Prevot, C. Baiocchi, M. C. Brussino, E. Pramauro, P. Savarino, V. Augugliaro, G. Marc and L. Palmisano, *Environ. Sci. Technol.*, 2001, **35**, 971–976.
- 3 X. Li, Y. Cheng, S. Kang and J. Mu, *Appl. Surf. Sci.*, 2010, **256**, 6705–6709.
- 4 M. Shao, L. Cheng, X. Zhang, D. D. D. Ma and S.-T. Lee, *J. Am. Chem. Soc.*, 2009, **131**, 17738–17739.
- 5 N. O. Gopal, H.-H. Lo and S.-C. Ke, *J. Am. Chem. Soc.*, 2008, **130**, 2760–2761.
- 6 C. Hu, T. Peng, X. Hu, Y. Nie, X. Zhou, J. Qu and H. He, *J. Am. Chem. Soc.*, 2010, **132**, 857–862.
- 7 S. Chen, W. Zhao, W. Liu and S. Zhang, *Appl. Surf. Sci.*, 2008, **255**, 2478–2484.
- 8 X. Shu, J. He and D. Chen, *Ind. Eng. Chem. Res.*, 2008, **47**, 4750–4753.
- 9 Z. Wang, B. Huang, Y. Dai, X. Qin, X. Zhang, P. Wang, H. Liu and J. Yu, *J. Phys. Chem. C*, 2009, **113**, 4612–4617.
- 10 H. Pan, Y.-W. Zhang, V. B. Shenoy and H. Gao, *ACS Catal.*, 2011, **1**, 99–104.
- 11 X. Wang, K. Maeda, A. Thomas, K. Takane, G. Xin, J. M. Carlsson, K. Domen and M. Antonietti, *Nat. Mater.*, 2009, **8**, 76–80.
- 12 S. C. Yan, Z. S. Li and Z. G. Zou, *Langmuir*, 2009, **25**, 10397–10401.
- 13 K. Maeda, X. Wang, Y. Nishihara, D. Lu, M. Antonietti and K. Domen, *J. Phys. Chem. C*, 2009, **113**, 4940–4947.
- 14 Q. Xiang, J. Yu and M. Jaroniec, *J. Phys. Chem. C*, 2011, **115**, 7355–7363.
- 15 S. C. Yan, Z. S. Li and Z. G. Zou, *Langmuir*, 2010, **26**, 3894–3901.
- 16 M. Xu, L. Han and S. Dong, *ACS Appl. Mater. Interfaces*, 2013, **5**, 12533–12540.
- 17 L. Sun, X. Zhao, C.-J. Jia, Y. Zhou, X. Cheng, P. Li, L. Liu and W. Fan, *J. Mater. Chem.*, 2012, **22**, 23428–23438.
- 18 Y. Zang, L. Li, Y. Zuo, H. Lin, G. Li and X. Guan, *RSC Adv.*, 2013, **3**, 13646–13650.

- 19 Y. Wang, X. Bai, C. Pan, J. He and Y. Zhu, *J. Mater. Chem.*, 2012, **22**, 11568–11573.
- 20 T. Li, L. Zhao, Y. He, J. Cai, M. Luo and J. Lin, *Appl. Catal., B*, 2013, **129**, 255–263.
- 21 S. Wang, D. Li, C. Sun, S. Yang, Y. Guan and H. He, *Appl. Catal., B*, 2014, **144**, 885–892.
- 22 K. Santosh, T. Surendar, K. Bharat, B. Arabinda and S. Vishnu, *J. Phys. Chem. C*, 2013, **117**, 26135–26143.
- 23 Z. Xiu, H. Bo, Y. Wu and X. Hao, *Appl. Surf. Sci.*, 2014, **289**, 394–399.
- 24 P. S. Braterman, Z. P. Xu and F. Yarberry, Layered double hydroxides, in *Handbook of Layered Materials*, ed. S. M. Auerbach, K. A. Carrado and P. K. Dutta, Marcel Dekker, Inc., New York, 2004, ch. 8, pp. 373–474.
- 25 G. R. Williams and D. O'Hare, *J. Mater. Chem.*, 2006, **16**, 3065–3074.
- 26 G. Fan, F. Li, D. G. Evans and X. Duan, *Chem. Soc. Rev.*, 2014, **43**, 7040–7066.
- 27 Á. Patzkó, R. Kun, V. Hornok, I. Dékány, T. Engelhardt and N. Schall, *Colloids Surf., A*, 2005, **265**, 64–72.
- 28 A. Mantilla, F. Tzompantzi, J. L. Fernández, J. A. I. Díaz Góngora and R. Gómez, *Catal. Today*, 2010, **150**, 353–357.
- 29 A. Mantilla, F. Tzompantzi, J. L. Fernández, J. A. I. Díaz Góngora, G. Mendoza and R. Gómez, *Catal. Today*, 2009, **148**, 119–123.
- 30 G. Fan, W. Sun, H. Wang and F. Li, *Chem. Eng. J.*, 2011, **174**, 467–474.
- 31 X. Xiang, L. Xie, Z. Li and F. Li, *Chem. Eng. J.*, 2013, **221**, 222–229.
- 32 Y. Zhao, F. Li, R. Zhang, D. G. Evans and X. Duan, *Chem. Mater.*, 2002, **14**, 4286–4291.
- 33 J. Luo, H. D. Jang, T. Sun, L. Xiao, Z. He, A. P. Katsoulidis, M. G. Kanatzidis, J. M. Gibson and J. Huang, *ACS Nano*, 2011, **5**, 8943–8949.
- 34 A. Thomas, A. Fischer, F. Goettmann, M. Antonietti, J.-O. Müller, R. Schlögl and J. M. Carlsson, *J. Mater. Chem.*, 2008, **18**, 4893–4908.
- 35 H. Yan, Y. Chen and S. Xu, *Int. J. Hydrogen Energy*, 2012, **37**, 125–133.
- 36 S. Song, J. Tu, Z. He, F. Hong, W. Liu and J. Chen, *Appl. Catal., A*, 2010, **378**, 169–174.
- 37 S. Gazi, R. Ananthakrishn and N. D. P. Singh, *J. Hazard. Mater.*, 2010, **183**, 894–901.
- 38 L. Pan, J. J. Zou, X. Zhang and L. Wang, *J. Am. Chem. Soc.*, 2011, **133**, 10000–10002.
- 39 J. W. Liu, G. Chen, Z. H. Li and Z. G. Zhang, *J. Solid State Chem.*, 2006, **179**, 3704–3708.
- 40 J. Hou, R. Cao, Z. Wang, S. Jiao and H. Zhu, *J. Mater. Chem.*, 2011, **21**, 7296–7301.
- 41 X. Zheng, S. Meng, J. Chen, J. Wang, J. Xian, Y. Shao, X. Fu and D. Li, *J. Phys. Chem. C*, 2013, **117**, 21263–21273.
- 42 S. Ge and L. Zhang, *Environ. Sci. Technol.*, 2011, **45**, 3027–3033.
- 43 K. Parida, L. Mohapatra and N. Baliarsingh, *J. Phys. Chem. C*, 2012, **116**, 22417–22424.
- 44 J. Mu, B. Chen, M. Zhang, Z. Guo, P. Zhang, Z. Zhang, Y. Sun, C. Shao and Y. Liu, *ACS Appl. Mater. Interfaces*, 2012, **4**, 424–430.
- 45 J. Kim, C. W. Lee and W. Choi, *Environ. Sci. Technol.*, 2010, **44**, 6849–6854.
- 46 M. R. Hoffmann, S. T. Martin, W. Choi and D. W. Bahnemann, *Chem. Rev.*, 1995, **95**, 69–96.
- 47 G. Li, K. H. Wong, X. Zhang, C. Hu, J. C. Yu, R. C. Y. Chan and P. K. Wong, *Chemosphere*, 2009, **76**, 1185–1191.